Ceramics International 43 (2017) 9600–9615

Contents lists available at ScienceDirect

Ceramics International

journal homepage: www.elsevier.com/locate/ceramint

A comprehensive mechanism for the sintering of plasma-sprayed nanostructured thermal barrier coatings

Guang-Rong Li, Guan-Jun Yang*, Cheng-Xin Li, Chang-Jiu Li

State Key Laboratory for Mechanical Behavior of Materials, School of Materials Science and Engineering, Xi'an Jiaotong University, Xi'an, Shaanxi Province 710049, PR China

ARTICLE INFO

Keywords:
Nanostructured coatings
Plasma-spraying
Thermal barrier coatings
Sintering
Two-stage kinetics

ABSTRACT

Nanostructured thermal barrier coatings (TBCs) are being widely researched for their superior thermal barrier effect and strain compliance. However, the sintering occurs inevitably in nanostructured TBCs that comprise both nanozones and lamellar zones, although the mechanism of sintering in such bimodal coatings is not yet clear. This study investigates the changes in microstructure and properties of nanostructured TBCs during thermal exposure with the aim to reveal the sintering mechanism operative in these coatings. Results show that the sintering process occurs in two stages. It was found that in the initial shorter stage (~0–10 h), the properties increased rapidly; moreover, this change was anisotropic. The main structural change was the significant healing of the intersplat pores through multiconnection. During the subsequent longer stage, the change in the properties was much smaller, where it was observed that the pores continued to heal, albeit at a much lower rate. Furthermore, the faster densification of the nanozones induced during sintering became significant, resulting in an opening at the interface between the nanozones and the lamellar zones. In brief, the pore healing at the lamellar zones affects the properties, especially in the initial stage. The presence of nanozones has a positive effect in that the performance degradation during the overall thermal exposure is slowed down. An understanding of this competing sintering mechanism would enable the structural tailoring of nanostructured TBCs in order to increase their thermal insulation and thermal cycling lifetime.

1. Introduction

Over the past few decades, thermal barrier coatings (TBCs) have been widely used in both aero and land-based gas turbines to protect their hot-section metallic components (e.g., combustion cans, blades and vanes) against high temperature. The TBCs significantly reduce heat transfer from the hot gas to the surface of metal alloy parts, and consequently higher operating temperatures can be employed resulting in notably improved efficiency of the gas turbines. A typical TBC system is a multilayer structure, consisting of a thermally-resistant top-coat and an oxidation resistant bond-coat applied over a metal substrate [1,2]. Owing to its unique porous structure and its excellent overall performance, plasma-sprayed yttria-stabilized zirconia (PS-YSZ) continues to dominate the processing application of the top-coat, especially in land-based gas turbines [3–5]. The lamellar structure of this top-coat with connected intersplat pores and intrasplat cracks results in a half more drop in the through-thickness thermal conductivity [6–10] and in the in-plane elastic modulus [5,11–13] with respect to the corresponding properties of the bulk YSZ material.

The continued requirement for increased gas turbine efficiency means that there is an urgent demand for the development of advanced TBCs with enhanced durability and resistance to degradation at higher operating temperatures. Consequently, doped-YSZ [14] and new candidate materials [15] for the application of top-coat are increasingly being investigated. Nanostructured materials are potentially attractive in view of the fact that the mechanical performance of these materials (hardness, strength, ductility and toughness) can be considerably enhanced if grain sizes are reduced from conventional microlevel to the nanoscale (i.e., < 100 nm) [16–18]. As a result, plasma sprayed nanostructured YSZ coatings have been widely studied and reported [19–22].

The achievement of the desired performance level of the nanostructured YSZ coatings depends crucially on their special microstructure that is inherent to plasma spraying. One of the biggest challenges is to retain the preexisting nanostructure of the feedstock [23]. Plasma spraying proceeds by the successive deposition of fully and partially molten particles on a substrate followed by lateral flattening, rapid solidification and cooling [24,25]. The fully molten nanostructured feedstock exhibits the traditional behavior of solidification, nucleation and growth [26], resulting in typical lamellar structure (lamellar zones)

* Corresponding author.
E-mail address: ygj@mail.xjtu.edu.cn (G.-J. Yang).

http://dx.doi.org/10.1016/j.ceramint.2017.04.083
Received 6 November 2016; Received in revised form 28 March 2017; Accepted 13 April 2017
Available online 14 April 2017

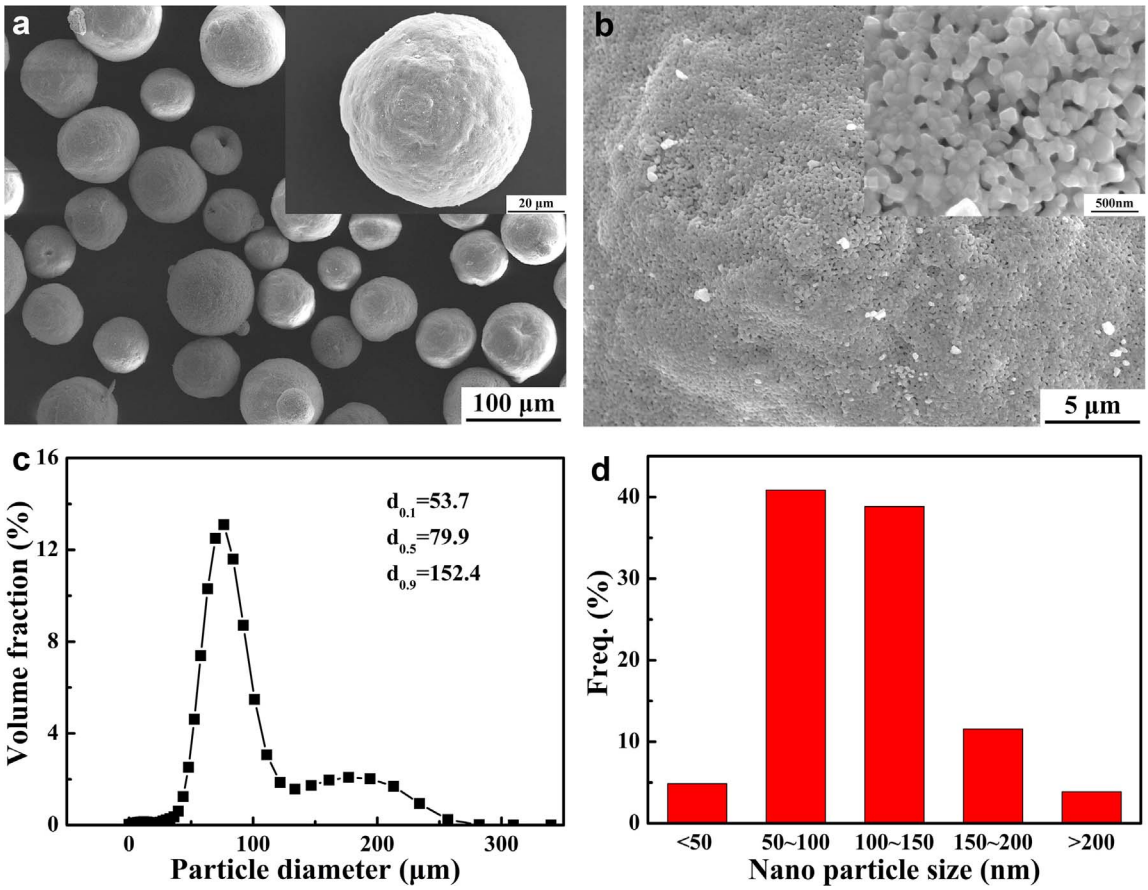

Fig. 1. Morphologies and size distributions of the agglomerates and the nanosized powders: (a) morphology of the agglomerates; (b) surface morphology of the agglomerates with nanosized powders; (c) size distribution of the agglomerates and (d) size distribution of the nanosized primary particles.

Table 1
Plasma spray parameters for the deposition of individual splats and coatings.

Parameters	Individual splats	Coatings
Plasma arc voltage / V	60	60
Plasma arc current / A	650	650
Flow rate of primary gas (Ar) / L min^{-1}	80	80
Flow rate of secondary gas (H_2) / L min^{-1}	16	16
Flow rate of powder feeding gas (N_2)/ L min^{-1}	4.5	4.5
Spray distance / mm	110	110
Torch traverse speed / mm s^{-1}	1000	500
Preheating temperature (°C)	300	/

[24,27]. However, this fully molten zone is often deleterious to the original nanostructure of the feedstock. Thus, the presence of the partially molten feedstock is necessary to translate the excellent physical properties of the nanostructured feedstock to the coatings. The fully molten zone facilitates sufficient particle adhesion and cohesion, and thus acts as a kind of matrix to the coating, whereas the semi-molten zone preserves the nanostructure. As a result, the integrity of the coating is maintained due to the fact that the semi-molten zones are surrounded by the fully molten zones, which act as binders. This morphology has been commonly described as a bimodal microstructure in previous reports [28,29]. In brief, in nanostructured YSZ coatings, the typical lamellar structure and the embedded-nanostructure coexist; in such a structure, the performance and the sintering behavior of the coating are intimately related to the presence of the conventional YSZ coating as well as to the nanostructured particles.

It is clear that the properties of the nanostructured YSZ coating are intrinsically associated with the degree of melting of the feedstock. Therefore, the coating performance is highly sensitive to the spraying parameters, which determine the melting degree. A key issue is to control the powder temperature in the thermal spray jet, which should be only slightly higher than the melting point of the material. Lima et al. [22,29] investigated the effect of spraying parameters on the percentage of the semi-molten zones. Moreover, the obtained bimodal structure depended to a great extent on the microhardness. The relatively lower hardness of the semi-molten zones contributed considerably to the excellent global mechanical properties. In addition to the spraying parameters, the powder size distribution also affects the resulting microstructure [23]. A broad particle size distribution, where a certain proportion of nanozones can be maintained, is more advantageous when compared to a narrow particle size distribution.

This optimal bimodal structure contributes to the superior reliability and lifetime of nanostructured TBCs with respect to conventional TBCs. It has been widely reported that nanostructured TBCs are potentially promising to achieve higher thermal cycling lifetime both for isothermal cycling [30–32] and gradient thermal cycling [33]. Regarding the sintering behavior of nanostructured TBCs, the faster densification in nanozones induced by sintering partially counteracts the degradation effect caused by pore-healing in the matrix zones [34,35]. The reason for this is that the nanozones have a higher surface area with a loose structure when compared to the matrix. The faster shrinking rate of the nanozones results in the formation of coarse pores at the boundary between the nanozone and the matrix. This mechanism is responsible mainly for the durable thermal insulating property during thermal exposure. However, there has been very little work carried out on the sintering behavior of nanostructured TBCs with bimodal structure.

The features of the bimodal nanostructured YSZ coatings in the as-deposited state can be summarized as follows: (i) the matrix is formed from the initially molten but subsequently solidified particles. The

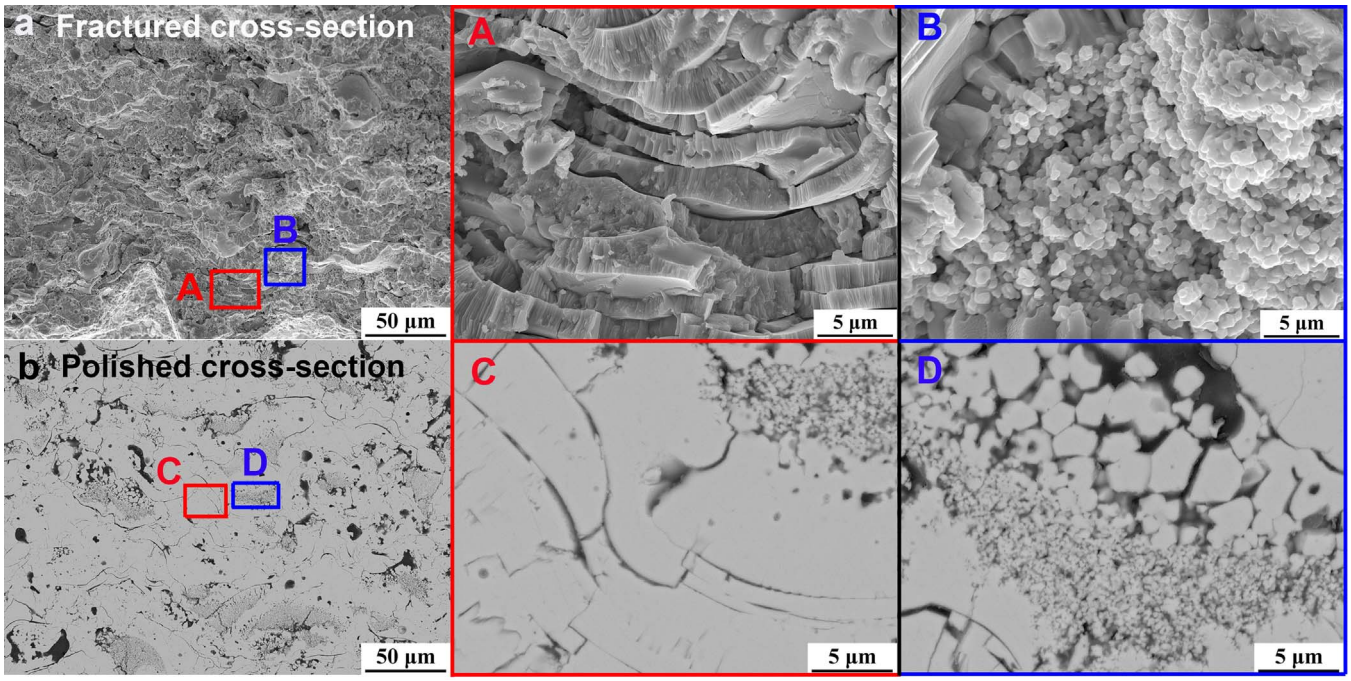

Fig. 2. Morphology of the as-deposited coatings: (a) Fractured cross-section. (A) and (B) show the magnified images of the zones corresponding to the red and blue boxes in (a), respectively; (b) polished cross-section. (C) and (D) show the magnified images of the zones corresponding to the red and blue boxes in (b), respectively.

inner structure of the splat has a high density after resolidification from the molten state. However, similar to the conventional PS YSZ coatings [13,27], the stacking of the splats leads to the formation of a lamellar structure with an interconnected 2-dimensional (2D) pore network. Intersplat pores correspond to imperfect bonding between layers, while intrasplat cracks are formed during quenching process. These 2D pores play a dominant role in determining the thermal insulation [8] and strain tolerance [13] of the structure; (ii) the nanozones exhibit a loose structure with a large quantity of microvoids. During thermal exposure, due to the isotropic microstructure of the powder material, the sintering mechanism of nanozones is similar to that observed in conventional ceramic sintering or that described in powder metallurgy [36]. However, the sintering of the matrix is much more structure- and material- specific owing to the anisotropy of the thermally sprayed coatings [12,37]. The lamellae are formed with columnar grains oriented along the direction of heat flow during the solidification of the molten droplets [38]. The differences in grain orientation and pore shape result in a distinctly different sintering mechanism for TBCs when compared to the powder-metallurgic material sintering. In short, the lamellar zones and the nanozones may follow different sintering mechanisms.

Wang et al. [21] reported that the grain size of a nanostructured zirconia coating increased linearly with increase in annealing time, suggesting that the activation energy is constant during the entire sintering process. Wu et al. [39] further confirmed that the nanostructure was gradually lost when the heat treatment was prolonged beyond a certain duration (> 10 h) at 1200 °C. Therefore, a certain incubation time is needed before the effect from the sintering of the nanozones begins to inhibit performance degradation. However, it is worth noting that the initial thermal exposure often leads to a much sharper increase in thermal conductivity and elastic modulus [34,39], although the mechanism behind is not clear. Consequently, in addition to the different sintering mechanisms that are operative, the competition between the effects from the sintering of the lamellar zones and the nanozones may modify the observed performance at different stages of thermal exposure. A comprehensive understanding of the sintering mechanism of the nanostructured TBCs is thereby necessary.

The objective of this study is to reveal the comprehensive mechanism of sintering operative in bimodal nanostructured TBCs. A systematical study of the changes in microstructure and properties during thermal exposure at various temperatures was carried out, following which the sintering mechanisms of the lamellar zones and the nanozones were revealed. The competing sintering effect of the lamellar zones and the nanozones at different stages of thermal exposure is also discussed. This fundamental study would help in the tailoring of optimized structures for advanced nanostructured TBCs.

2. Experimental procedure

2.1. Materials

A commercial nanostructured 7 wt% YSZ (Nanox S4007, Inframat corporation, Farmington, CT, USA) was used as the feedstock in this study, which is produced through a spray drying process to agglomerate individual nanosized YSZ powders into microscopic agglomerates. The size distribution of the agglomerates was evaluated using a laser diffraction particle size analyzer (Beckman Coulter, Miami, FL, USA), and the size distribution of the nanopowders was measured by Nano measurer. The morphologies and particle size distribution of the agglomerates and the nanosized powders are shown in Fig. 1. It is seen that the agglomerates are spherical and that the particle size range is in a range of 50–150 μm, as shown in Fig. 1(a, c). When examined at a higher magnification, it can be observed that the agglomerates are porous and formed by the agglomeration of individual nanosized YSZ particles with most of the diameters varying from 50 to 150 nm, as shown in Fig. 1(b, d).

2.2. Sample preparation and thermal exposure

To observe and characterize their sintering behavior, 1 mm thick nanostructured YSZ coatings were plasma sprayed on a stainless steel substrate without special preheating. A free-standing YSZ sample was obtained by dissolving the substrate in a hydrochloric acid solution followed by further immersing in deionized water for 24 h, with the aim to remove residual acid in the coating. Except for preheating of the substrate to approximately 300 °C, the same parameters as the coating

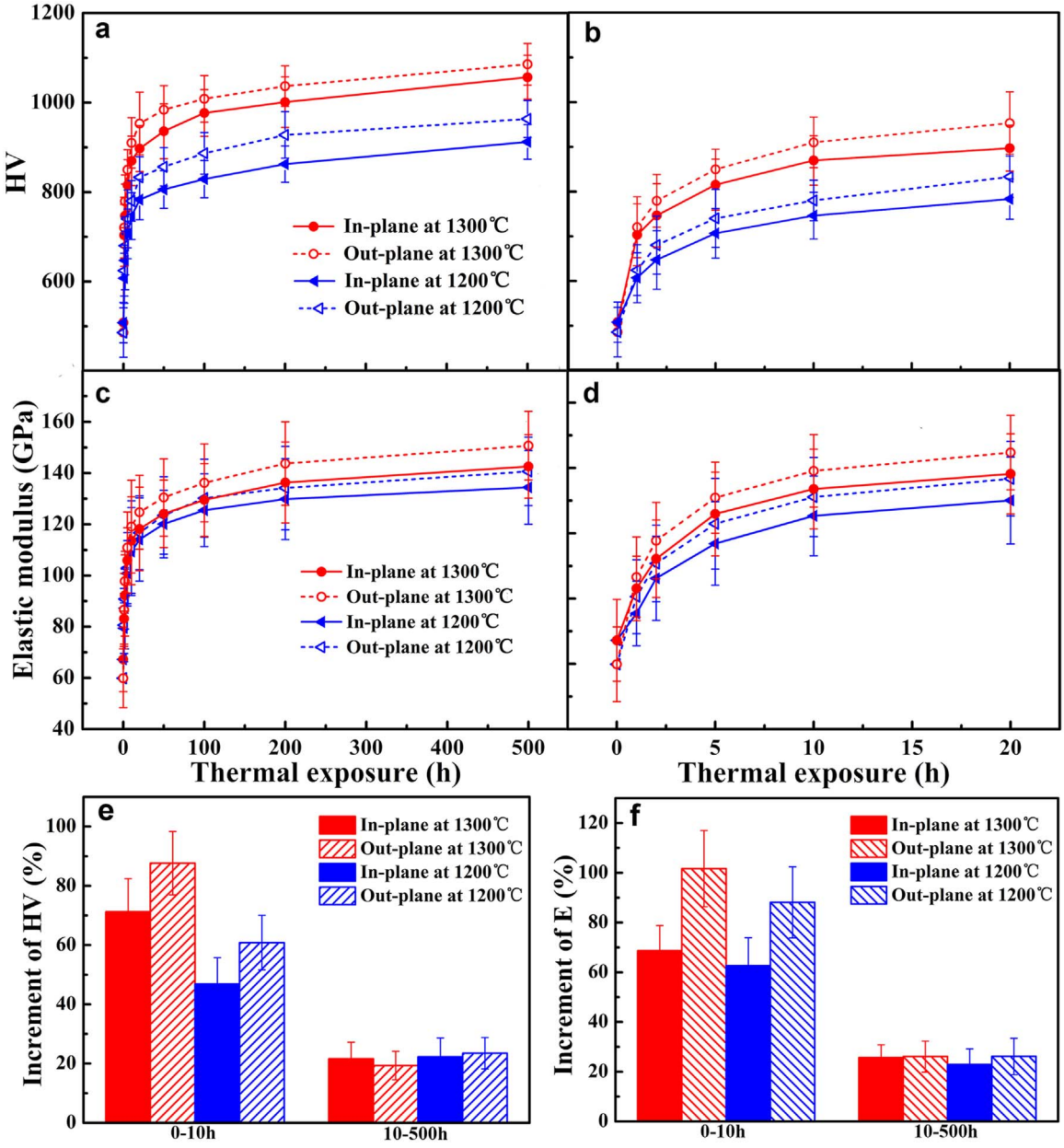

Fig. 3. Evolution of mechanical properties during thermal exposure: (a, b, e) hardness and (c, d, f) elastic modulus. (e) and (f) refer to the increment of hardness and elastic modulus for different durations, respectively.

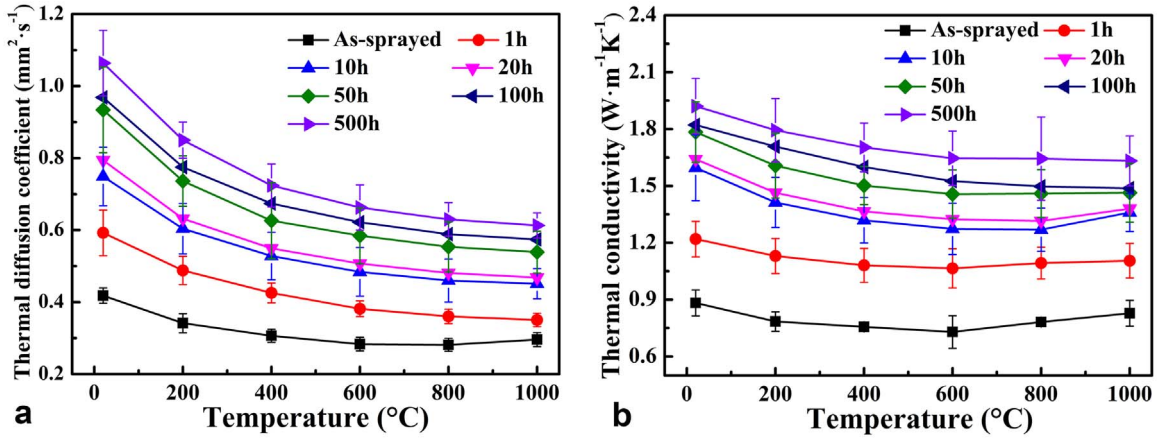

Fig. 4. Evolution of thermal properties after thermal exposure at 1300 °C: (a) thermal diffusivities measured from room temperature to 1000 °C; and (b) thermal conductivity.

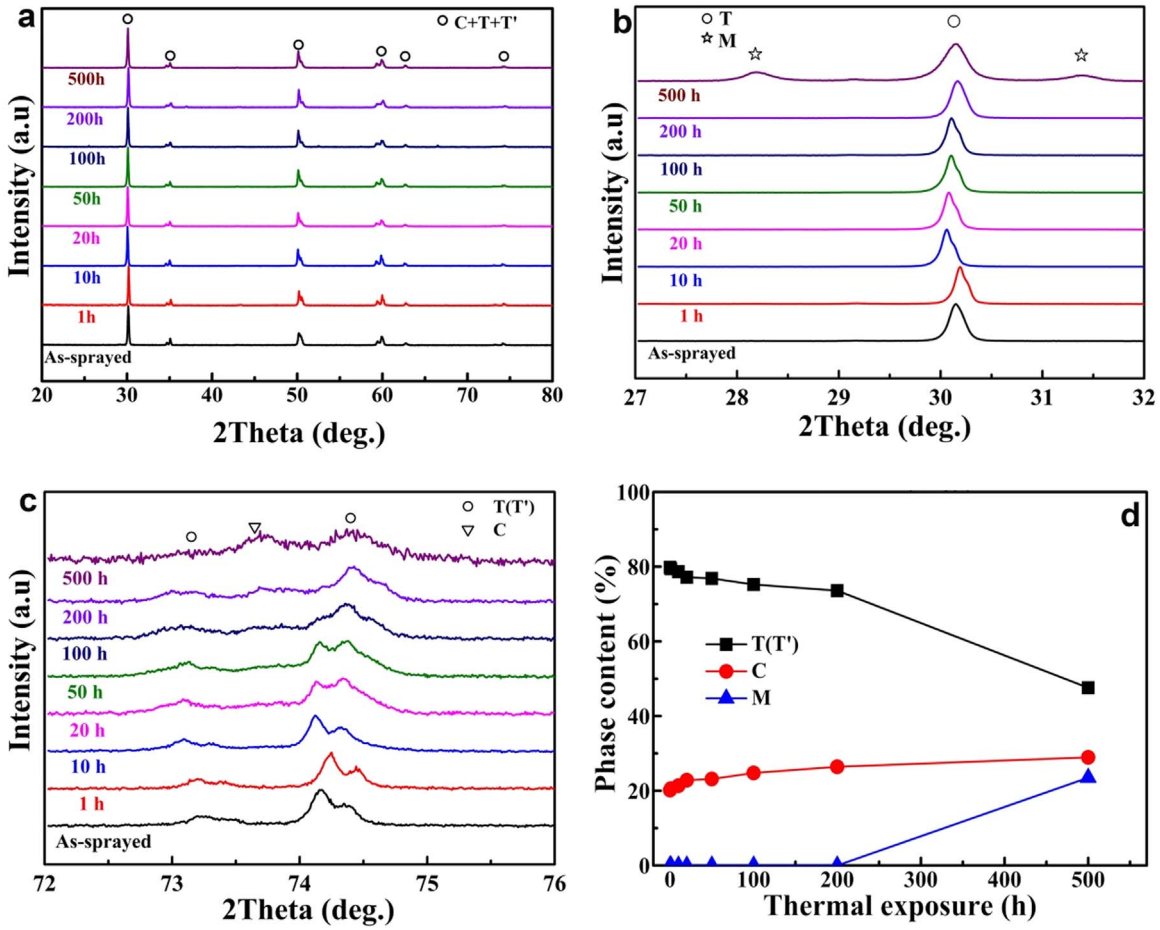

Fig. 5. XRD patterns of the nanostructured YSZ coatings before and after thermal exposure in the 2θ range from (a) 20–80°, (b) 27–32°, and (c) 72–76°; and (d) change of the phase contents with thermal exposure duration.

deposition were used to deposit individual splats in order to examine the sintering behavior of the lamellae in YSZ coatings. A sintered 8 wt% YSZ with a polished surface was used as the support for splat deposition. The surface temperature during spraying was monitored with the help of a pyrometer (RAYR312ML3U, Raytek, Santa Cruz, CA). The details of the set-up for preheating can be found elsewhere [25]. It is reported that the melting point of 7–8 wt%YSZ is approximately 2700 °C [34]. The plasma spray parameters were chosen based on a previous report [33], so as to obtain a bimodal microstructure with both lamellar zones and nanozones, as shown in Table 1.

The service temperature of TBCs for gas turbine (e.g., F-class land-based gas turbine) is ~1000 °C with a lifetime of approximately 8000–24000 h [40]. In order to speed up the testing, samples were heated in a furnace to higher temperatures of 1200 °C and 1300 °C, with the aim to shorten the heating duration. The samples were held at the heating temperature for progressively increasing durations, after which they were cooled down to room temperature. To avoid unexpected structural degradation in coatings by fast temperature change, the heating and cooling rates were fixed at a relatively low rate of 10 °C/min.

2.3. Microstructure characterization

The surface and cross-sectional morphology of the coatings were examined using a scanning electron microscopy (SEM) system (TESCAN MIRA 3, Czech). Atomic force microscopy (AFM, Asylum Research Cypher, USA) was used to examine the surface morphology of individual splats, which actually correspond to the surface of intersplat pores. Optical microscopy system was used to pre-position the sample during in-situ observations on the domain of the same splat after different durations of thermal exposure. The apparent porosity of the coatings after heating was determined by image analysis using SEM backscattered electron imaging (BEI) on the polished cross-section at a magnification of ×1000. For each coating, at least ten images were used to estimate the porosity. It is believed that 2D pores play a dominant role in determining the thermal and mechanical properties of plasma sprayed ceramic coatings [8,13]. Accordingly, in addition to the apparent porosity, residual 2D pore length densities (including intersplat pores and intrasplat cracks) after different thermal exposure durations were also determined. The densities of intersplat pores and intrasplat cracks were obtained, respectively, from the polished cross-section and surface of the coatings. For each state, at least 20 SEM images taken at a magnification of ×5000 were used. More details on the measurement of the 2D pore length density can be found elsewhere [41].

X-ray diffraction analysis (XRD, Rigaku D/max-2400, Japan) was used to characterize the crystalline structure of both as-sprayed and aged coatings. The scanning rate was 5°/min and the phase contents were estimated from the relative intensity ratios by using following equations:

$$C_M = \frac{0.82\{I_M(11\bar{1}) + I_M(111)\}}{0.82\{I_M(11\bar{1}) + I_M(111)\} + I_{T,C}(111)} \quad (1)$$

$$C_T = (1 - C_M)\frac{1.14\{I_T(400) + I_T(004)\}}{1.14\{I_T(400) + I_T(004)\} + I_C(400)} \quad (2)$$

$$C_C = 1 - (C_M + C_T) \quad (3)$$

where C refers to the phase content, I is the diffraction peak intensity, subscripts refer to the different phases, M, T and C refer to monoclinic,

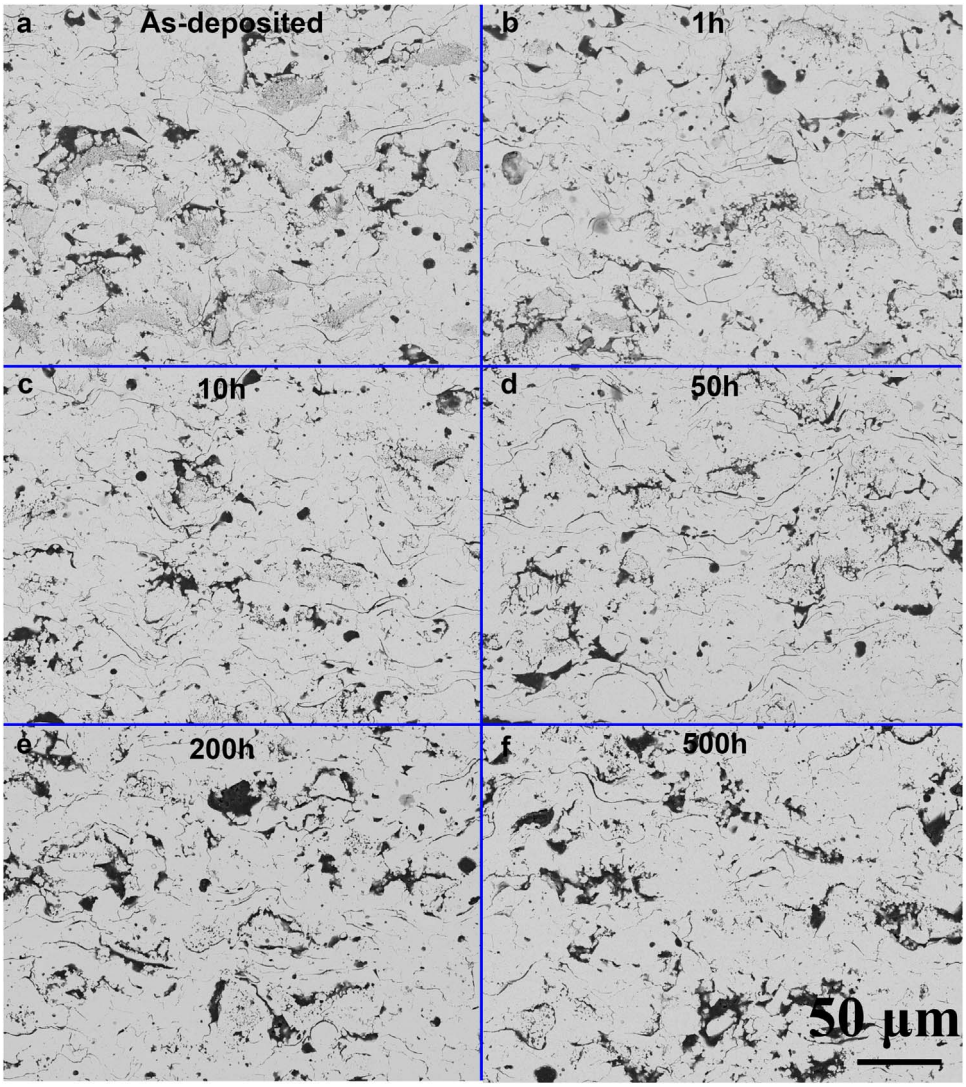

Fig. 6. Evolution of the polished cross-section of nanostructured YSZ coatings with increasing thermal exposure duration.

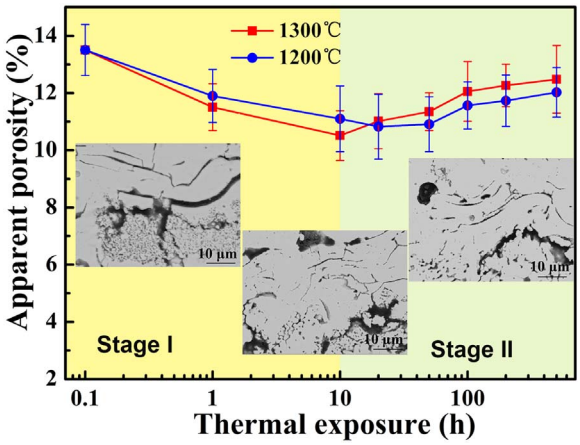

Fig. 7. Evolution of the apparent porosity after progressively increasing durations in thermal exposure.

tetragonal, and cubic phases, respectively. Slower scanning at 1°/min was performed in the ranges of 27–32° and 72–76°, to clearly identify the diffraction peaks arising from the cubic and tetragonal phase.

2.4. Property measurement

Knoop indentation (Buehler Micromet 5104, Akashi Corporation, Japan) at a test load of 300 gf and a holding time of 30 s was used to obtain the elastic modulus of YSZ coatings in both the in-plane and out-plane directions [11]. The sample size used for the measurement of thermal conductivity was Φ12.7×1 mm. The thermal diffusivity of YSZ coatings was measured with a laser flash analyzer (Netzsch, Germany) in the temperature range from room temperature to 1000 °C. Each measurement was repeated three times to minimize errors. The heat capacity of the coatings was determined by differential scanning calorimetry 404 (Netzsch, Germany) and the density was calculated by dividing the mass of the sample by its volume. The thermal conductivities were then calculated using the following equation [7,42]:

$$\lambda = \rho \cdot C_P \cdot \alpha \quad (4)$$

where λ is the calculated thermal conductivity, ρ is the density, C_P is the heat capacity, and α is the thermal diffusivity.

3. Results

3.1. Microstructure of the as-deposited coatings

Fig. 2 shows the microstructure of the as-deposited coatings. In the

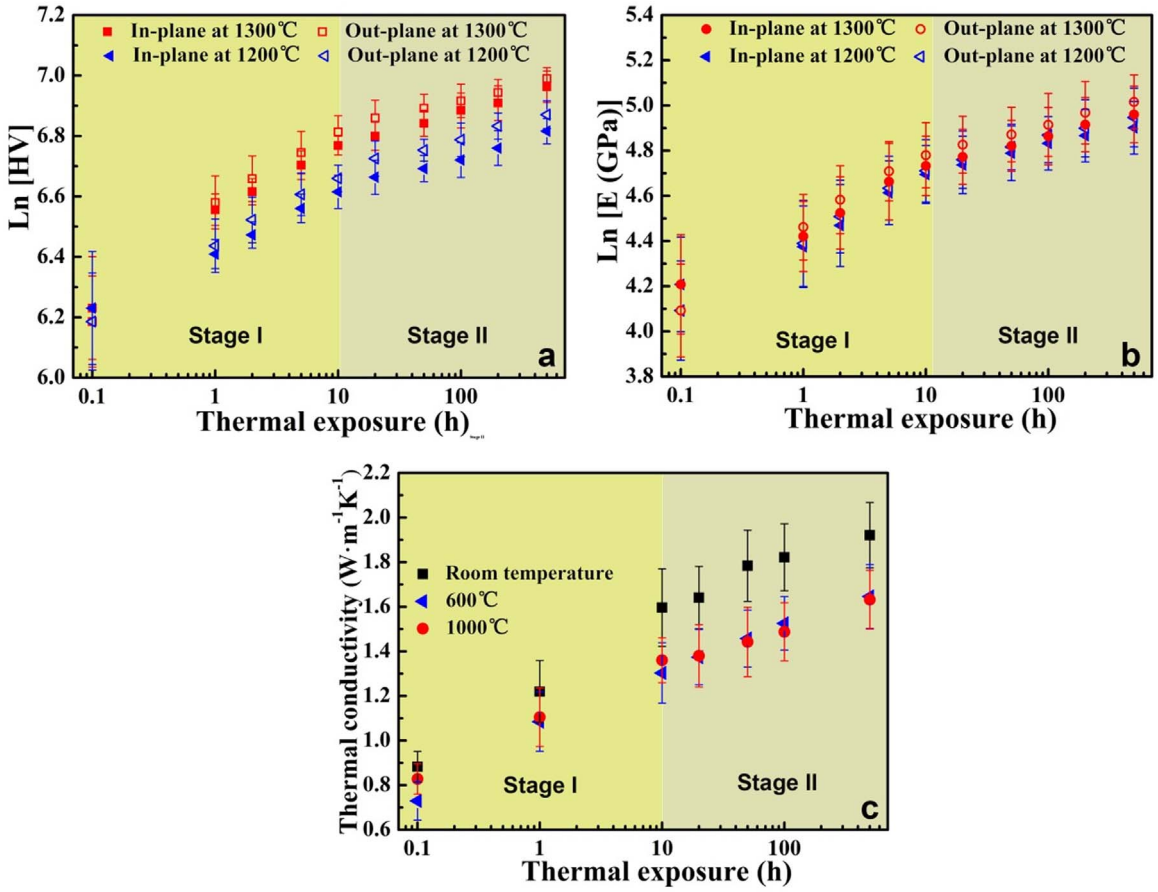

Fig. 8. Two-stage evolutionary trend in properties: (a) hardness; (b) elastic modulus; and (c) thermal conductivity measured at room temperature, 600 °C and 1000 °C. (a) and (b) were obtained from Fig. 3, whereas (c) was obtained from Fig. 4.

fractured cross-section of the YSZ coatings (see Fig. 2a), it can be observed that the porous nanozones were surrounded by the lamellar zones, indicating that the coating presents a bimodal structure similar to that reported in previous studies [22,29]. It is possible to recognize the similarities between the nanozone and the morphology of feedstock; this suggests that the nanozones were retained from the unmolten or semimolten nanostructured agglomerated feedstock during the spray process. The lamellar zones exhibit similar morphology to the coatings produced from conventional microsized YSZ feedstock [6,13], since the solidification, nucleation and growth of these fully molten powders are similar. Columnar grains oriented along the deposition direction can be clearly seen in the splats. In the polished cross-section, the nanozones and the lamellar zones can be recognized as dark and light zones (see Fig. 2b), respectively. The percentage area of the nanozones embedded in the coatings was estimated to be approximately 25%. In contrast, the apparent porosity of the as-deposited coatings was 13%. In addition to the nanozones and the lamellar zones, some fine equiaxed grains were also formed as a result of homogeneous nucleation and precipitation from an undercooled melt (see Fig. 2(b–D)). The estimated cooling rate of plasma-sprayed coatings is of the order of 10^6 K/s [20,38]. It is believed that homogeneous nucleation resulted in the formation of fine grains owing to a high nucleation rate and a low growth rate.

3.2. Evolution of mechanical and thermal properties during thermal exposure

Fig. 3 shows the evolution of the mechanical properties of nanostructured YSZ coatings after thermal exposure for different intervals of time. To begin with, the changes in hardness and elastic modulus show a similar trend. This trend shows that a much higher increase rate in mechanical properties at initial thermal exposure stage slows down dramatically during the following extended thermal exposure stage. That means the sintering kinetics of the nanostructured YSZ coatings vary with the duration of thermal exposure, which may result from the special bimodal structure. Secondly, the increment of elastic modulus at the initial shorter stage was significantly larger than that at the subsequent longer stage, as shown in Fig. 3(e, f). Finally, the elastic modulus of the as-deposited coatings shows a clear anisotropy with a larger in-plane value with respect to the out-plane value. However, after thermal exposure, the increment in the out-plane elastic modulus is often greater than that of the in-plane elastic modulus.

Fig. 4 shows the evolution of the thermal diffusion coefficient and thermal conductivity of the nanostructured YSZ coatings after different thermal exposure durations. The thermal conductivity was calculated from (Eq. (4)). It can be observed that the thermal diffusion coefficients decrease slightly as a function of the measured temperature values. Moreover, similar to the mechanical properties, the thermal diffusion coefficients increase significantly after thermal exposure, as shown in Fig. 4(a). A similar trend can be found for thermal conductivity. This is consistent with the results for APS YSZ coatings in previous reports [33,43]. The temperature-dependent thermal conductivity data have been discussed with respect to the heat transfer mechanisms operative in TBC coatings. A TBC coating can be considered as a two-phase system made from the splat and the gas trapped within the pores. In the presence of gas filling the pores, it is reported that the heat transfer is affected by the pore dimension (L) and the mean free path of molecules (λ) in the gas phase, which in turn is a function of temperature and pressure [44]. In plasma-sprayed TBCs, the pore thickness is comparable to λ (~100 nm) at ambient temperature and

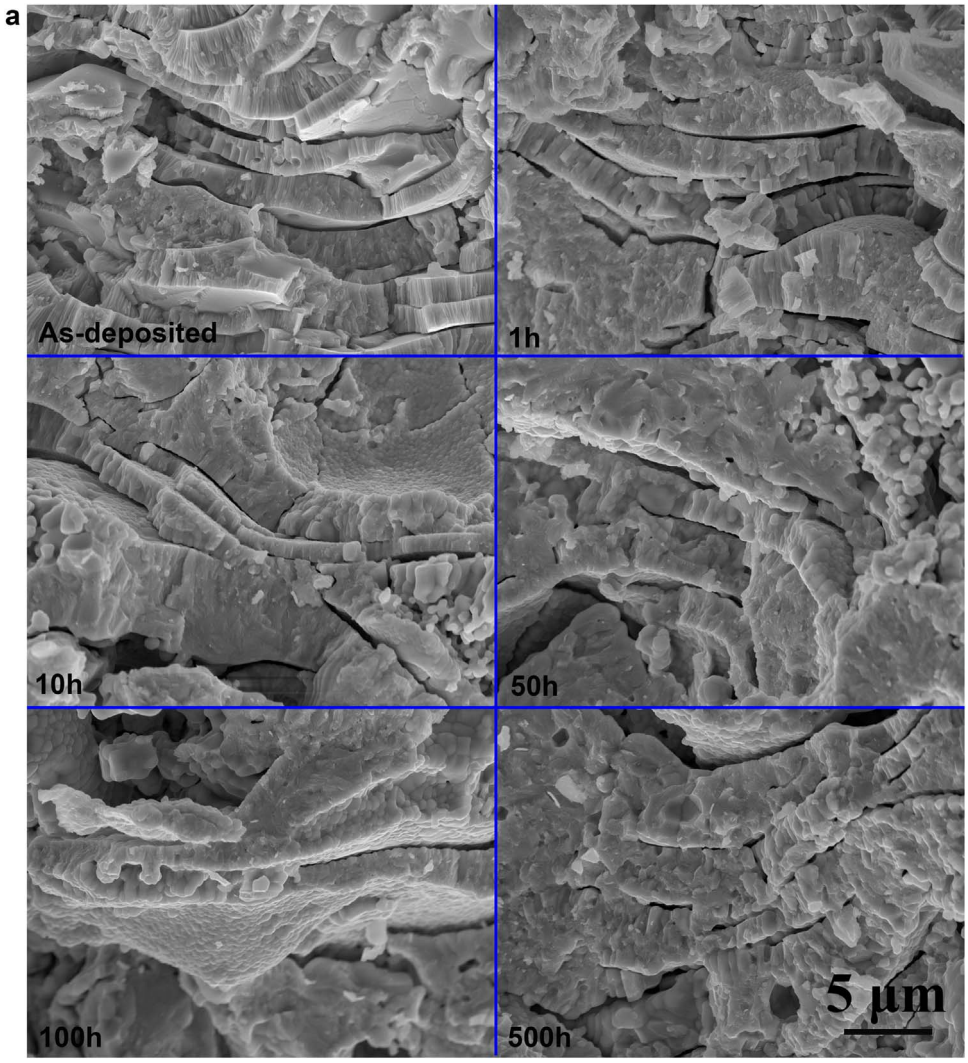

Fig. 9. Morphological evolution of the fractured cross-section and surface in lamellar zones after various thermal exposure durations: (a) fractured cross-section and (b) surface.

pressure, which means that convection can be neglected [45]. Moreover, the gas conductivity in a pore is close to that in the free gas (e.g., ~0.025 W m^{-1} K^{-1}), only provided that the dimensions of the pore are much larger than the mean free path ($L > \sim 10\lambda$). Given the pore dimension in typical TBCs ($L < \sim 1$ μm) [6,13], the conductivity in the pores should be significantly lower than that of the free gas**.** Of course, all gas conductivities are much lower than those of solids. In the case of a splat, the heat transfer occurs primarily through phonon transport owing to the fact that there are almost no free electrons [45]. Therefore, it can be concluded that the heat flux within the coatings includes conventional phonon conduction through splats, collision conduction in the gas, and radiative heat transfer [46]. At lower temperatures, heat conduction occurs only through phonon transport. As the temperature increases, phonon scattering becomes stronger, and the thermal conductivity of the material decreases. However, when the temperature is further increased (e.g., above 700 °C), radiation becomes significant. As a result of these combined effects, the thermal conductivity decreases to a minimum with increase in measured temperatures, and subsequently increases only slightly at higher temperatures.

3.3. Effect of thermal exposure on the microstructure

Fig. 5 shows the XRD patterns of the nanostructured coatings before and after thermal exposure at 1300 °C, given that significant phase transformation can occur in samples treated at higher temperatures (i.e., > 1200 °C) [40,47,48]. The as-sprayed coating showed primarily tetragonal phase, together with a small fraction of cubic phase, which is consistent with previous reports [40,48–50]. Since the cooling rate of the splat during plasma spraying is extremely high, both phase equilibrium (between tetragonal and cubic phases at temperatures > 560 °C) and the eutectoid phase transformation (from tetragonal phase to both monoclinic and cubic phases) cannot be completely achieved [40]. As a result, the tetragonal phase, composed of 7YSZ, is retained within the splats after cooling down. According to the equilibrium phase diagram, 7YSZ should be composed of both monoclinic phase and cubic phase [51]. It is obvious that the 7YSZ-formed tetragonal phase is a thermodynamically metastable phase, which is often named as the non-equilibrium tetragonal phase or nontransformable tetragonal phase (T′). Quantitative calculations of the phase contents shown in Fig. 5d indicate that after thermal exposure at 1300 °C, distinct phase changes can be observed. During thermal exposure, the redistribution of Y element resulted in the formation of equilibrium tetragonal and cubic phases [47,49,52]. Consequently, the content of cubic phase increased gradually with increase in thermal exposure duration. When the samples were cooled down from the exposed temperature (i.e., 1300 °C) to room temperature, the eutectoid reaction at 560 °C led to the phase transformation from the equilibrium tetragonal phase to both monoclinic and cubic phases [51]. However, this eutectoid reaction is highly dependent on the effective

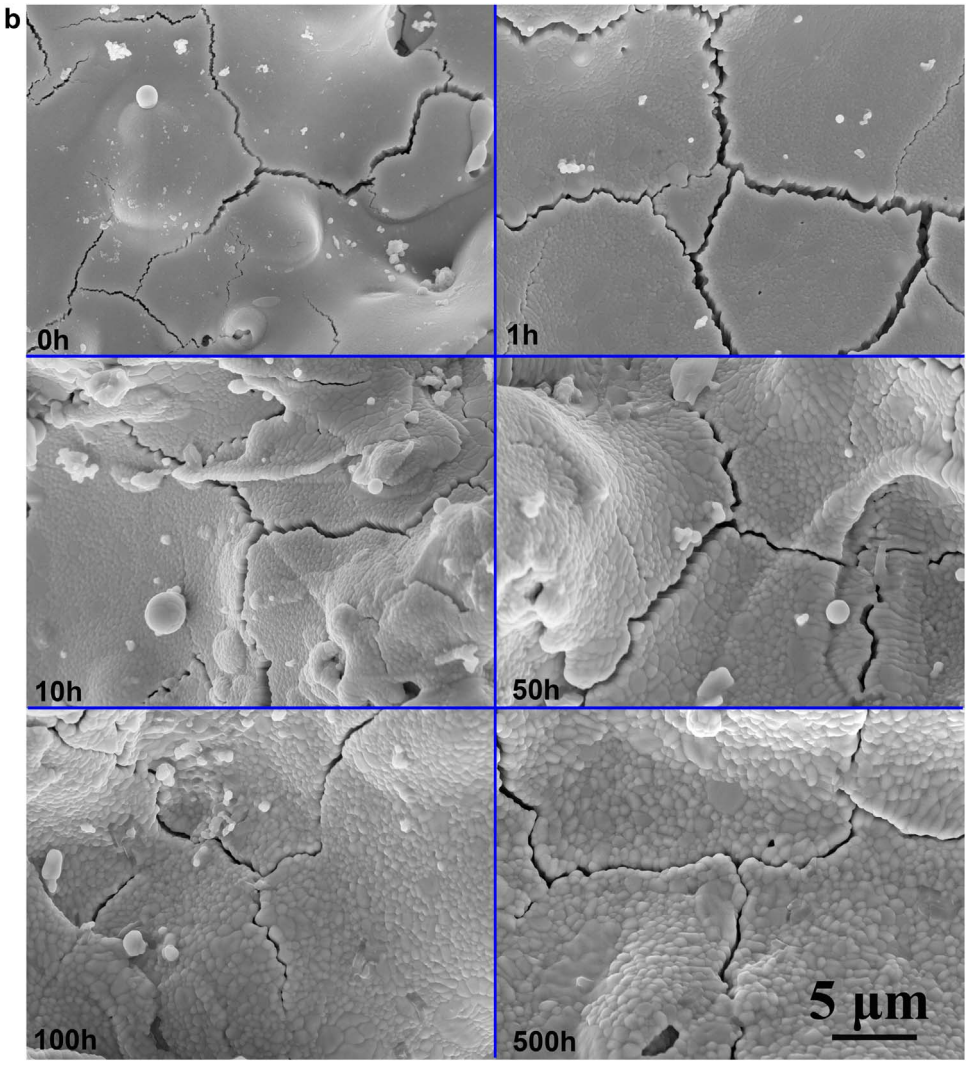

Fig. 9. (*continued*)

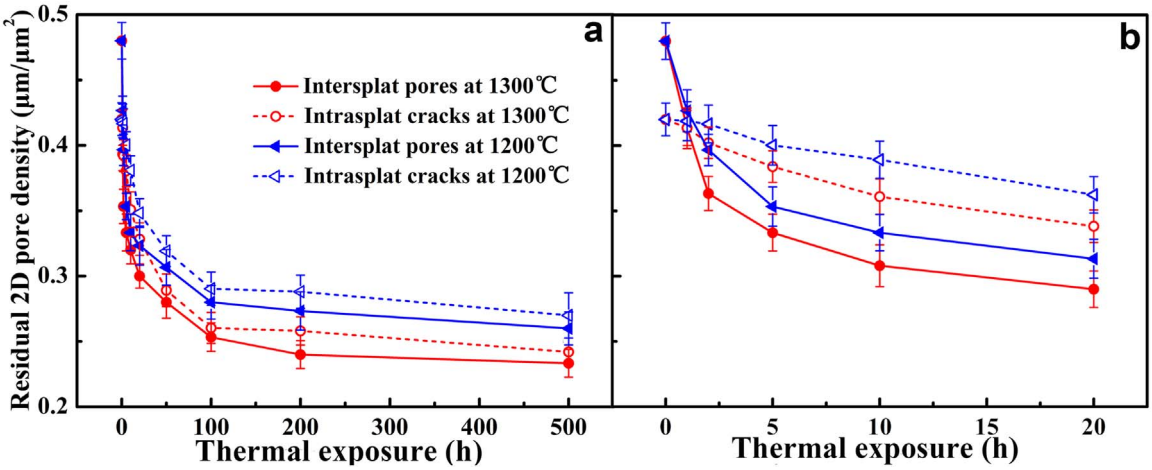

Fig. 10. Evolution of the 2D pore length density as a function of thermal exposure durations: (a) 0–500 h and (b) 0–20 h.

diffusion of Y element, which is achieved through the thermal vibration of the Y^{3+} ion. At a relatively low temperature (i.e., 560 °C), the thermal vibration of ions becomes less intensive. Therefore, the formation of the monoclinic phase becomes clearly visible only after a relatively long duration (see Fig. 5d).

Fig. 6 shows the polished cross-section of YSZ coatings after progressively increasing thermal exposure durations. In the case of the as-deposited state, a bimodal structure with a distinct contrast can be observed, where the dark nanozones are surrounded by the lighter lamellar zones. With increase in thermal exposure duration, this contrast was not as distinct as in the as-deposited state. Sintering occurred both in the lamellar zones and in the nanozones.

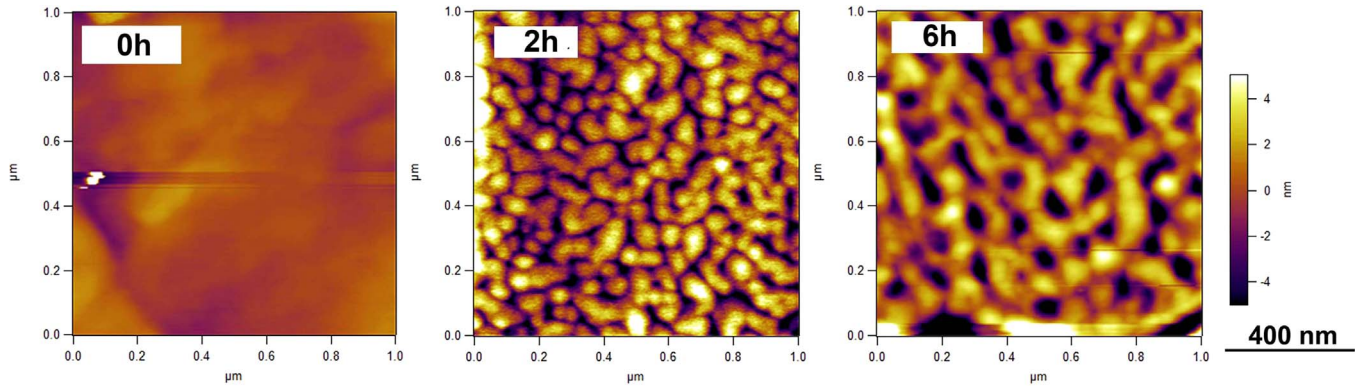

Fig. 11. Morphological changes on the surface of an individual splat after thermal exposure at 1200 °C.

Consequently, the 2D pores were healed significantly in the lamellar zones, while the grains grew to neck-connect with each other in the nanozones. The change in apparent porosity after thermal exposure is shown in Fig. 7. It can be found that the apparent porosity decreases during the initial thermal treatment (< 10 h). After a longer thermal treatment (> 100 h), the apparent porosity exhibits a slight increase. This observation suggests that the sintering of lamellar zones and nanozones may compete during the overall thermal exposure.

4. Discussion

4.1. Two-stage evolution trend of properties

PS YSZ coatings often have elastic modulus and thermal conductivity values, which are approximately less than half of those corresponding properties of bulk YSZ [5,6,53]. Moreover, in the as-deposited state, the mechanical and thermal properties in the out-plane direction are lower than that in the in-plane direction [12,37]. During thermal exposure, both the mechanical properties and the thermal conductivity increased dramatically at the initial duration, after which the increase rate slowed down significantly when the duration was extended (see Fig. 3). This suggests that the sintering kinetics is strongly related to the thermally activated structural changes at different durations.

Fig. 8 shows that there are two distinct stages in the evolution of properties. More specially, in Fig. 8(a, b), a Ln-t curve corresponding to the evolution of mechanical properties shown in Fig. 3 is given. Fig. 8c shows the evolution of thermal conductivity as a function of thermal exposure duration. In order to show the overall evolution, 0.1 h was used to stand for the as-sprayed state (corresponding to 0 h). To begin with, a distinct two-stage trend in property evolution could be observed. The sintering kinetics in the initial stage of thermal exposure (~0–10 h, termed as Stage I) was much higher than that during the subsequent longer duration of thermal exposure (termed as Stage II). It appears therefore that most of the increase in properties occurs already in the Stage I (~ 70%) with respect to the total observed increase during the overall thermal duration. In addition to the above-described stage-sensitive sintering kinetics, another noteworthy phenomenon was the anisotropy in the evolution of mechanical properties. The increase rate of the mechanical properties in the out-plane direction was higher than that in the in-plane direction, in particular, in the initial stage (see Fig. 8(a, b) and Fig. 3(a, b)). Correspondingly, increase in mechanical properties in the out-plane direction was greater than that in the in-plane direction (see Fig. 3(e, f)). It is believed that the mechanical properties of PS YSZ coatings are dependent on the nature of the connected 2D pore network [13]. In the case of the nanostructured TBCs, the evolution of properties may be an overall result reflecting the changes in the microstructure of both lamellar and nanozones.

First, the pore healing behavior at the lamellar zones was investigated in detail to account for the observed stage-sensitive and anisotropic sintering kinetics during thermal exposure. Fig. 9 shows the morphological evolution of fractured cross-section and surface lamellar zones after thermal exposure. If the overall thermal duration is considered, pore healing could be clearly observed, despite in the intersplat pores and the intrasplat cracks. Consequently, the lamellar structure present in the as-deposited state disappeared gradually, whereas the splat was stiffened by the healing of intrasplat cracks; this phenomenon is consistent with observations reported in previous investigations [5,6] carried out with the aim to obtain coatings with lower the surface areas [54]. Qualitatively, the macroscale structural evolution is responsible for the increase in both the mechanical properties [13] and the thermal property [8] during overall evolution (see Figs. 3 and 4). When considering the initial stage (0–10 h) with a higher sintering kinetics, it can be observed that the healing of intersplat pores is more significant than that of the intrasplat cracks. The corresponding evolution of the statistical 2D pore length density as a function of thermal duration time is shown in Fig. 10. The densities of both the intersplat pores and the intrasplat cracks decreased significantly during the overall duration of thermal exposure. However, in the Stage I, the decrease in intersplat pores was much more pronounced than that of the intrasplat cracks. Consequently, the healing of intersplat pores is the dominant structural change at this stage (0–10 h), which is responsible for the anisotropic evolution of mechanical properties. The reason for this is that the healing of intersplat pores results in an increase in the interlamellar bonding ratio, which has a significant effect on the elastic modulus in both in-plane and out-plane directions [13,24]. That's why both the in-plane and the out-plane mechanical properties increased during the Stage I (see Fig. 3). However, it is reported that the elastic modulus is more sensitive to its corresponding vertical cracks [55]. As a result, the increase in mechanical properties in the out-plane direction is greater than that in the in-plane direction, as shown in Fig. 3(e, f).

4.2. Stage I: Enhanced sintering kinetics induced by multiconnection of intersplat pores

Based on the above results, the ultrafast sintering kinetics observed in the Stage I is attributed primarily to the significant healing of intersplat pores in the lamellar zones. For this zone, the splat-formed lamellar structure and the columnar grains inside individual splats were clearly seen (see Fig. 9). It is reported that the columnar grains arise from nucleation at splat boundary followed by rapid growth into the molten splat [38]. Consequently, most of the columnar grains are parallel to the deposition direction.

In order to investigate the pore healing behavior, the surfaces of individual splats were considered to serve as the intersplat pore surfaces, since the two surfaces of a pore are actually either the top surface or the bottom surface of an individual splat with columnar

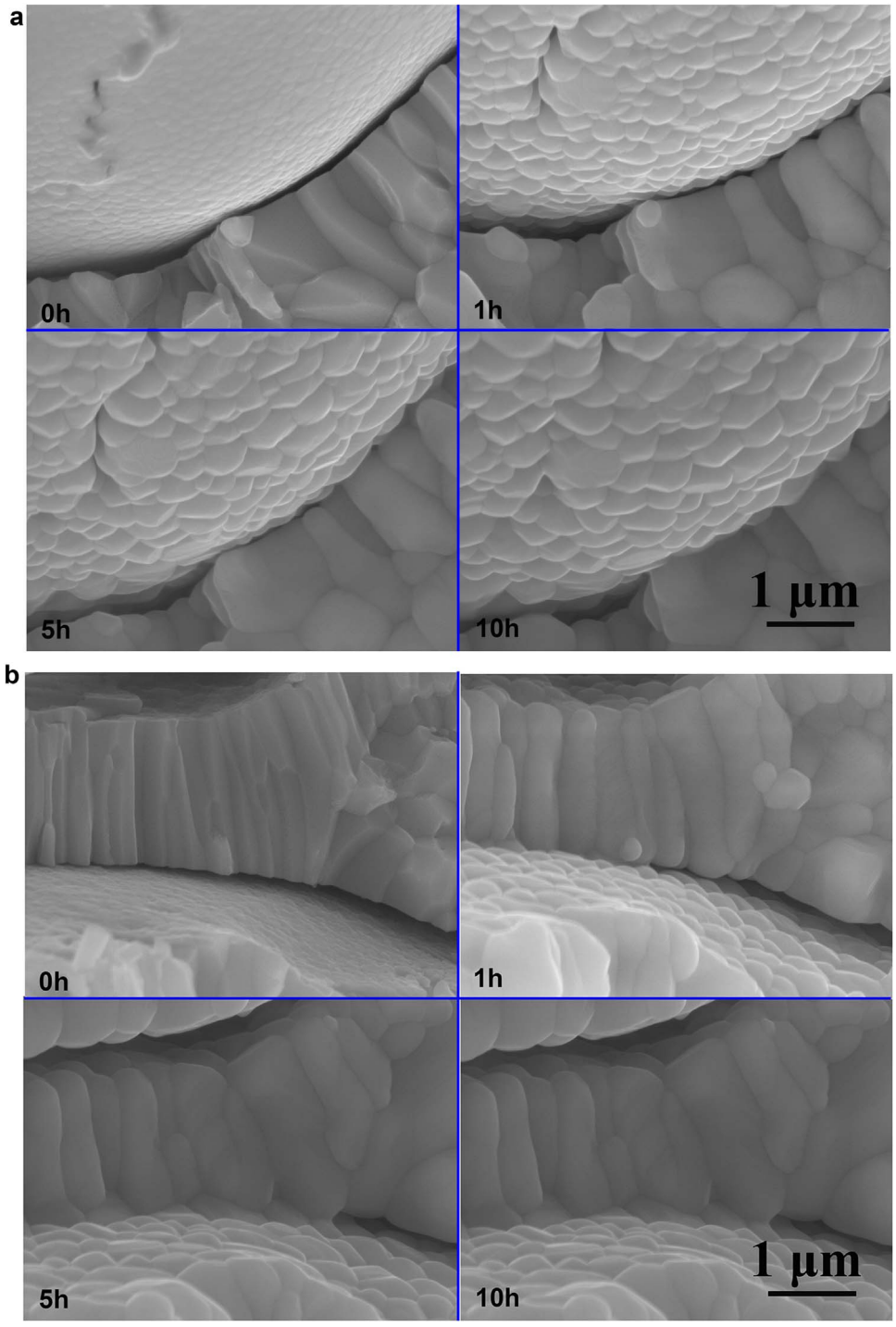

Fig. 12. Multiconnection-induced healing of intersplat pore tips after thermal exposure at different temperatures: (a) 1200 °C and (b) 1300 °C.

grains. Fig. 11 shows the in-situ changes in the surface morphology of an individual splat obtained from AFM after thermal exposure for different durations. It can be observed that the relatively smooth surface became roughened stemming from different mechanisms, i.e., faceting of the grain surface, grooving of the bared grain boundary and columnar grains convex. These different mechanisms lead to different levels of roughening. To sum up, during thermal exposure, the smooth surfaces of intersplat pores are roughened to different extents, depending upon the mechanism of roughening.

It is widely believed that the intersplat bonding ratio in the plasma-sprayed ceramic coatings is approximately 10–32% for the case with no special preheating on substrate [24,56–58]. This means that the intersplat pores partially separate the two neighboring layers owing to the limited bonding areas. Consequently, nearly all intersplat pores have tips. However, the intrasplat cracks arise from the quenching stage to release stress [59]. As a result, the intrasplat cracks often completely separate the splat segments in one layer. Therefore, the number of intersplat pore tips is much greater with respect to that of the intrasplat cracks. Moreover, the columnar grains often grow along the deposition direction. Extremely narrow intersplat pore tips may have a higher possibility to be healed, resulting in ultrafast sintering kinetics. Fig. 12 shows the in-situ healing behavior of intersplat pores. It can be observed that the smooth intersplat pore surface evolves to become roughening. This is consistent with the AFM profiles observed

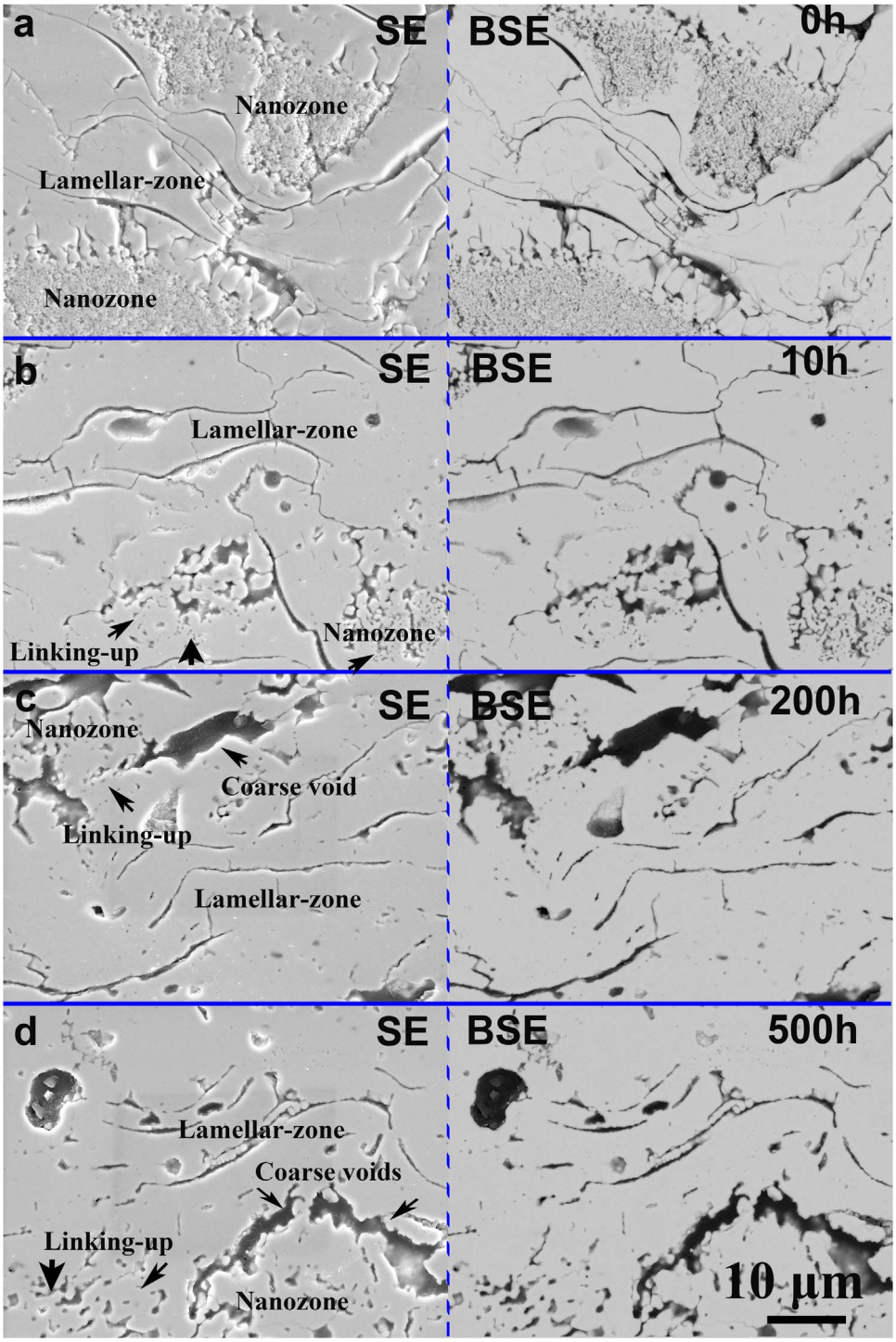

Fig. 13. Evolution of the interface between the lamellar zones and the nanozones during thermal exposure.

in Fig. 11. Moreover, the healing of intersplat pores began at the pore tips. Owing to the multiscale roughening mechanism, the counter surfaces of pore tips were bridge-connected to finish the healing procedure. It is reported that according to conventional ceramic sintering or powder metallurgy theories, sintering processes begin with the connection of particles through single-neck connections [36]. Different from the conventional mechanism, thermal exposure leads to the multiscale roughening on the surfaces of intersplat pores (see Fig. 11). At pore tips, the multiscale roughening results in multipoint connection of the counter surfaces. The sintering process is accompanied by a decrease in free energy of the whole system. The multipoint bridging significantly decreases the free energy of the system, which contributes to the ultrafast sintering kinetics during the Stage I.

To sum up, the multiconnection between splats, induced by thermally-activated multiscale roughening mechanisms, leads to a significant healing of intersplat pores during the Stage I of thermal exposure. This could be essentially responsible for the very severe and anisotropic mechanical evolution observed in Fig. 8. This phenomenon may be contradicted to our initial perception, since nanozones always present a higher sintering kinetics than fully molten zones [34,60,61] owing to their higher surface energy. However, the unique structure of PS YSZ coatings complicates this condition due to the large amount of

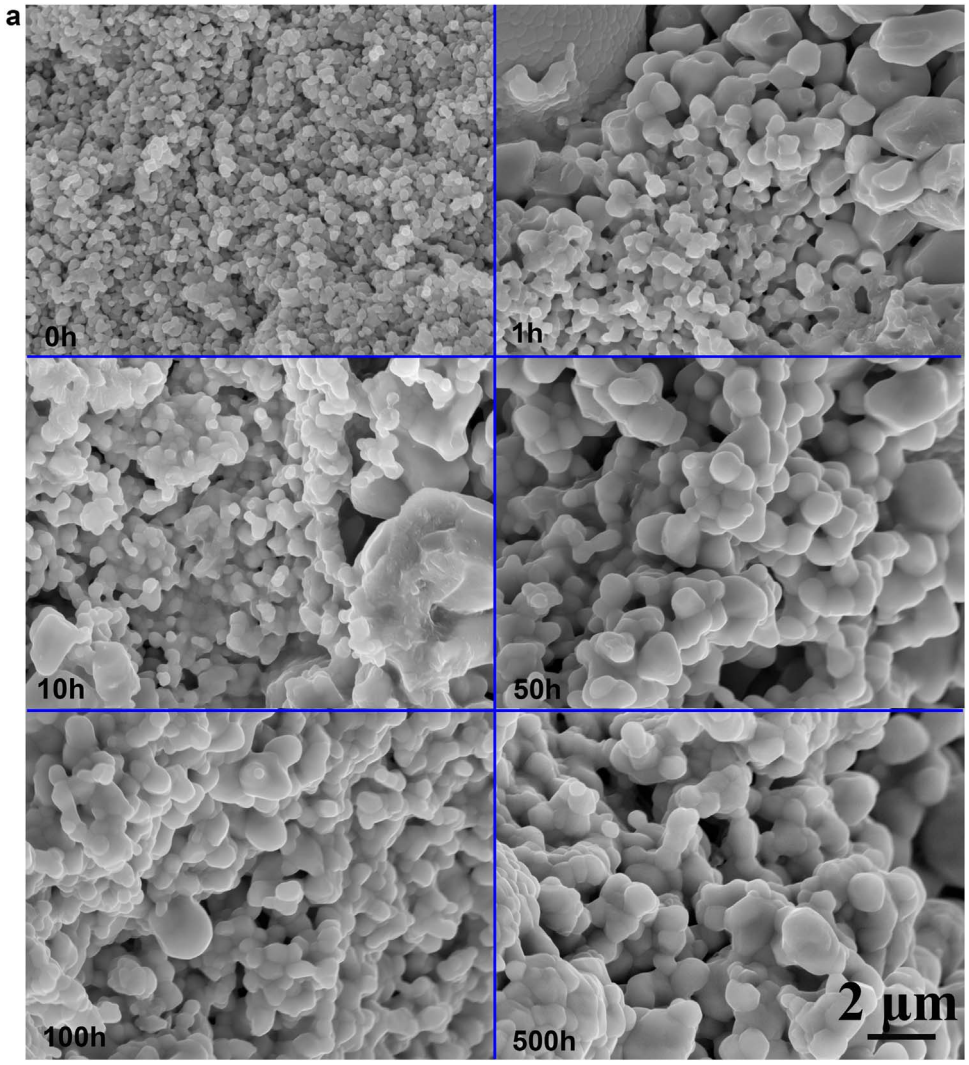

Fig. 14. Evolution of the nanozones after thermal exposure for different durations at 1300 °C: (a) morphological evolution; (b) grain size distribution.

2D pores, which predominantly determine the evolution of properties. Consequently, the multiconnection-induced enhanced healing of intersplat pores contributes primarily to the initial untrafast sintering kinetics that results in a dramatic property increase.

4.3. Stage II: Sintering of nanozones

In conventional plasma-sprayed YSZ coatings, the multiconnection-induced enhanced sintering kinetics leads to the healing of narrow parts (i.e., pore tips) in Stage I. After this stage, the multiconnection between surfaces is hindered by the residual wider parts of the intersplat pores. Consequently, pore healing only can proceed primarily from two sides to the center, as described in a previous study [27]. In parallel, the intrasplat cracks begin to heal (see Fig. 10). However, the healing rates of both the residual intersplat pores and the intrasplat cracks are slower in the Stage II than during the initial stage. As a result, a slower sintering kinetics is observed when the duration of thermal exposure is extended. This is also applicable to the lamellar zones in the nanostructured YSZ coatings. This is the reason why some residual large intersplat pores and residual intrasplat cracks can still be observed in the polished cross-section and surface even after thermal exposure at 1300 °C for 500 h (see Figs. 6 and 9). However, the presence of nanozones in the nanostructured YSZ coatings also has a distinct effect on the evolution of structure and properties during long thermal exposure.

The nanozones are formed by embedding the porous nanostructured agglomerates in the matrix (lamellar-zones). Consequently, in addition to the typical pores existing in the conventional plasma-sprayed ceramic coatings [38,62], the nanostructured YSZ coatings introduce large quantity of micropores in the nanozones. These micropores have a positive effect on the thermal insulation performance [33–35]. It is reported that the activation energy of nanograin growth is much lower than that of bulk YSZ [21], since the presence of micropores increases the surface energy drastically. Consequently, from the view of sintering-induced densification, the porous nanozones exhibit a much higher driving force than that of the lamellar zones. Fig. 13 shows the interfacial evolution between lamellar zones and nanozones during thermal exposure. On the one hand, sintering leads to the linking-up of nanozones and the lamellar zones at some parts. Consequently, the nanozones decrease as a function of thermal exposure durations (see Fig. 6). This is consistent with a previous report [63]. On the other hand, the differential sintering rates (densification rates) may contribute to the formation of an opening at the interface between the porous nanozones and the matrix [34,35]. This may account for the observed change in apparent porosity (see Fig. 7). In the case of conventional plasma-sprayed ceramic coatings, the observed pores in the polished cross-section mainly arise from the spalling-off of the weakly bonded splats during sample preparation [64,65]. After thermal exposure, the lamellar bonding is enhanced significantly, as a result of which the apparent porosity decreases.

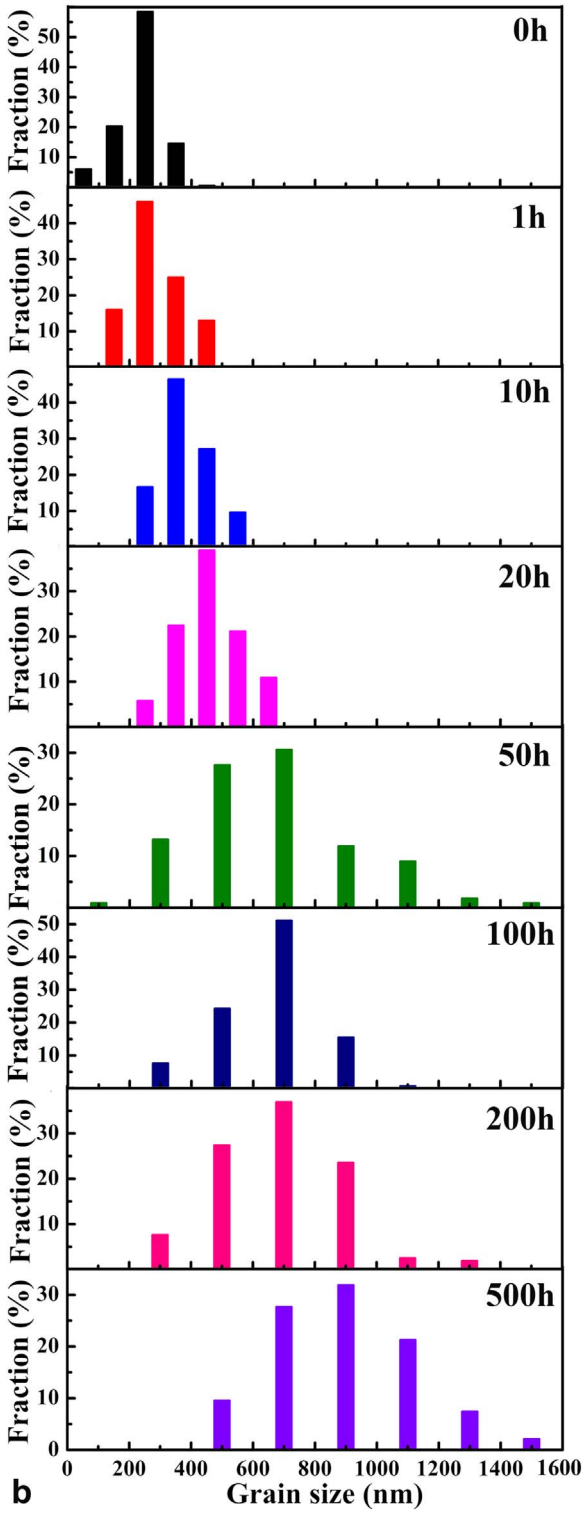

Fig. 14. (*continued*)

Based on the discussion in Sections 4.1 and 4.2, the distinctly improved bonding occurs mainly in Stage I. Correspondingly, the apparent porosity often decreases faster in this stage with respect to the following extended duration [6,40,47]. However, in the case of nanostructured coatings, thermal exposure leads to differential sintering rates for the nanozones and the lamellar zones. This results in the formation of coarse voids, which further contribute to the apparent porosity. Based on the combined mechanism of changes in the lamellar zones and nanozones, it is concluded that the apparent porosity decreased distinctly when initially exposed (Stage I), owing to the enhanced bonding between splats. Subsequently, the apparent porosity remained relatively stable and increased slightly after long duration (Stage II), as shown in Fig. 7. This is consistent with the observations reported in previous publications [34,35].

Fig. 14 shows the evolution of nanozones during thermal exposure. It can be found that there is significant grain growth as a function of duration. Consequently, the nanostructure disappeared gradually during thermal exposure. However, detailed observations showed that the grain growth is not as significant as in Stage I (i.e., < 10 h). From the grain size distribution, it is found that the grains grew only gradually as the thermal exposure duration was increased. This means that a significant change in the grain size distribution often needs a certain incubation period. This is consistent with a previous study [21], which demonstrated that the grain size becomes large than 100 nm after thermal exposure for 25 h at 1100 °C. In brief, though the surface energy of nanozones is much higher than the bulk YSZ, the sintering of these nanozones is still similar to the conventional ceramic, i.e., sintering through neck-connection of particles [36] and material transport occurs only through the neck between the particles. The whole process is accompanied by an increase in the neck diameter and shrinkage in the micropores. Consequently, the sintering-induced significant densification of the nanozones often needs an incubation period to be completed. This further confirms that the initial ultrafast sintering kinetics is primarily attributed to the multiconnection-induced enhanced pore healing in the lamellar zones.

In brief, the sintering mechanism of the nanostructured YSZ coatings actually reflects the combined behavior of the lamellar zones and the nanozones. At the lamellar zones, sintering leads to the significant healing of the 2D pores, particularly in the initial stage (Stage I). Consequently, the mechanical properties and the thermal property increase dramatically. At the nanozones, the much lower activated energy leads to a higher sintering-induced densification rate with respect to the lamellar zones. The opening at the interface of the lamellar zones and the nanozones counteracts the effect of the disappearance of micropores between nanoparticles. Consequently, the apparent porosity decreases in Stage I, and subsequently increases slightly owing to the appearance of coarse voids between the lamellar zones and the nanozones. Based on the above discussion, this comprehensive mechanism of sintering retards performance degradation [22,34,35] and enhances the thermal shock resistance [30–33].

By understanding the comprehensive sintering mechanism of nanostructured TBCs, it is possible to achieve structural tailoring toward advanced TBCs by inserting some larger scale interlamellar pores. During plasma spraying, some nanozones can be inserted inside the conventional lamellar coatings. Subsequently, thermal exposure leads to the faster and significant densification of the nanozones, leaving a few larger scale interlamellar pores. It is relatively difficult for these large interlamellar pores to be healed by multiconnection. Consequently, a highly sintering-resistant structure with increased thermal insulation and prolonged thermal cycling lifetime may be obtained.

5. Conclusions

In this study, the comprehensive sintering mechanism of plasma-sprayed nanostructured YSZ coatings was revealed. The as-deposited bimodal structure of the nanostructured YSZ coatings exhibited distinct two-stage sintering kinetics during thermal exposure. The lamellar zones and the nanozones significantly presented different sintering mechanisms. The changes in structure and properties were resulted from the combined effect of these two mechanisms. The conclusions of the study are as follows:

(i) The as-deposited nanostructured YSZ coatings exhibited a distinct bimodal structure, which depended on the degree of melting of the

feedstock. The nanozones (unmolten particles) were surrounded by the lamellar zones (molten zones). The area ratio of the nanozones was approximately 25%.

(ii) During thermal exposure, both mechanical and thermal property showed significant increase. Furthermore, the observed increase exhibited a clear two-stage trend. The rate of increase during the initial short stage (Stage I) is much higher than in the subsequent longer stage (Stage II).

(iii) In Stage I, an examination of the pore healing behavior revealed that the initial ultrafast sintering kinetics can be attributed primarily to the healing of intersplat pores induced by multi-connection. This leads to a dramatic increase in properties during this stage along with enhanced anisotropy.

(iv) In Stage II, in addition to further pore healing with a much slower kinetics at the lamellar zones, the differential sintering rates of the lamellar zones and the nanozones contribute to the formation of an opening at the interface of these two zones. More specifically, at the nanozones, the high activated energy of nanograins leads to significant grain growth during the overall duration of thermal exposure. The neck-connection of these grains resulting from sintering leads to a higher densification rate with respect to the matrix (lamellar zones). Consequently, some coarse voids appear at the weakly-bonded interface between the nanozones and the matrix. However, an incubation period is often necessary before this sintering-induced significant densification of the nanozones can take place.

In brief, in Stage I, the multiconnection induced healing of intersplat pores dominates the evolution of structure and properties. In Stage II, there is a distinct slowing down in the healing of pores. The nanograins grow gradually during the overall thermal exposure. The sintering-induced faster densification of nanozones becomes significant after a certain duration, which contributes to the apparent porosity and has a positive effect in inhibiting performance degradation. By revealing the comprehensive sintering mechanism of nanostructured YSZ coatings, this fundamental study contributes to the tailoring of the structure of TBCs to achieve the desired performance.

Acknowledgments

The present project was supported by the National Basic Research Program of China (No. 2013CB035701), the Fundamental Research Funds for the Central Universities, and the National Program for Support of Top-notch Young Professionals.

References

[1] J.T. Demasimarcin, D.K. Gupta, Protective coatings in the gas-turbine engine, Surf. Coat. Tech. 68 (1994) 1–9.
[2] T.V., M. Andritschky, W. Fischer, H.P. Buchkremer, D. Stover, Effects of deposition temperature and thermal cycling on residual stress state in zirconia-based thermal barrier coatings, Surf. Coat. Tech. 120 (1999), 1999, pp. 103–111.
[3] J.M. Drexler, K. Shinoda, A.L. Ortiz, D.S. Li, A.L. Vasiliev, A.D. Gledhill, S. Sampath, N.P. Padture, Air-plasma-sprayed thermal barrier coatings that are resistant to high-temperature attack by glassy deposits, Acta Mater. 58 (2010) 6835–6844.
[4] D.Y. Chen, M. Gell, E.H. Jordan, E. Cao, X.Q. Ma, Thermal stability of air plasma spray and solution precursor plasma spray thermal barrier coatings, J. Am. Ceram. Soc. 90 (2007) 3160–3166.
[5] J.A. Thompson, T.W. Clyne, The effect of heat treatment on the stiffness of zirconia top coats in plasma-sprayed TBCs, Acta Mater. 49 (2001) 1565–1575.
[6] S. Paul, A. Cipitria, S.A. Tsipas, T.W. Clyne, Sintering characteristics of plasma sprayed zirconia coatings containing different stabilisers, Surf. Coat. Tech. 203 (2009) 1069–1074.
[7] W.G. Chi, S. Sampath, H. Wang, Microstructure-thermal conductivity relationships for plasma-sprayed yttria-stabilized zirconia coatings, J. Am. Ceram. Soc. 91 (2008) 2636–2645.
[8] H. Xie, Y.C. Xie, G.J. Yang, C.X. Li, C.J. Li, Modeling thermal conductivity of thermally sprayed coatings with intrasplat cracks, J. Therm. Spray. Techn. 22 (2013) 1328–1336.
[9] I.O. Golosnoy, A. Cipitria, T.W. Clyne, Heat transfer through plasma-sprayed thermal barrier coatings in gas turbines: a review of recent work, J. Therm. Spray. Techn. 18 (2009) 809–821.
[10] I.O. Golosnoy, S. Paul, T.W. Clyne, Modelling of gas permeation through ceramic coatings produced by thermal spraying, Acta Mater. 56 (2008) 874–883.
[11] R.S. Lima, S.E. Kruger, G. Lamouche, B.R. Marple, Elastic modulus measurements via laser-ultrasonic and Knoop indentation techniques in thermally sprayed coatings, J. Therm. Spray. Technol. 14 (2005) 52–60.
[12] Y. Tan, A. Shyam, W.B. Choi, E. Lara-Curzio, S. Sampath, Anisotropic elastic properties of thermal spray coatings determined via resonant ultrasound spectroscopy, Acta Mater. 58 (2010) 5305–5315.
[13] G.R. Li, B.W. Lv, G.J. Yang, W.X. Zhang, C.X. Li, C.J. Li, Relationship between lamellar structure and elastic modulus of thermally sprayed thermal barrier coatings with intra-splat cracks, J. Therm. Spray. Technol. 24 (2015) 1355–1367.
[14] M. Zhao, W. Pan, Effect of lattice defects on thermal conductivity of Ti-doped, Y_2O_3-stabilized ZrO_2, Acta Mater. 61 (2013) 5496–5503.
[15] X.R. Ren, M. Zhao, C.L. Wan, Y.X. Zheng, W. Pan, High-temperature aging of plasma sprayed quasi-eutectoid $LaYbZr_2O_7$-Part I: phase evolution, J. Am. Ceram. Soc. 98 (2015) 2829–2835.
[16] M. Gell, Application opportunities for nanostructured materials and coatings, Mat. Sci. Eng. A-Struct. 204 (1995) 246–251.
[17] R.W. Siegel, Nanostructured materials - mind over matter, Nanostruct. Mater. 3 (1993) 1–18.
[18] Y.L. Lu, P.K. Liaw, The mechanical properties of nanostructured materials, Jom-J. Min. Met. Mat. S. 53 (2001) 31–35.
[19] H. Chen, C.X. Ding, Nanostructured zirconia coating prepared by atmospheric plasma spraying, Surf. Coat. Tech. 150 (2002) 31–36.
[20] Y. Zeng, S.W. Lee, L. Gao, C.X. Ding, Atmospheric plasma sprayed coatings of nanostructured zirconia, J. Eur. Ceram. Soc. 22 (2002) 347–351.
[21] N. Wang, C.N. Zhou, S.K. Gong, H.B. Xu, Heat treatment of nanostructured thermal barrier coating, Ceram. Int. 33 (2007) 1075–1081.
[22] R.S. Lima, B.R. Marple, Thermal spray coatings engineered from nanostructured ceramic agglomerated powders for structural, thermal barrier and biomedical applications: a review, J. Therm. Spray. Technol. 16 (2007) 40–63.
[23] R.S. Lima, A. Kucuk, C.C. Berndt, Integrity of nanostructured partially stabilized zirconia after plasma spray processing, Mat. Sci. Eng. A-Struct. 313 (2001) 75–82.
[24] C.J. Li, A. Ohmori, Relationships between the microstructure and properties of thermally sprayed deposits, J. Therm. Spray. Technol. 11 (2002) 365–374.
[25] G.J. Yang, C.X. Li, S. Hao, Y.Z. Xing, E.J. Yang, C.J. Li, Critical bonding temperature for the splat bonding formation during plasma spraying of ceramic materials, Surf. Coat. Tech. 235 (2013) 841–847.
[26] R. Mcpherson, A review of microstructure and properties of plasma sprayed ceramic coatings, Surf. Coat. Tech. 39 (1989) 173–181.
[27] A. Cipitria, I.O. Golosnoy, T.W. Clyne, A sintering model for plasma-sprayed zirconia TBCs. Part I: free-standing coatings, Acta Mater. 57 (2009) 980–992.
[28] M. Gell, E.H. Jordan, Y.H. Sohn, D. Goberman, L. Shaw, T.D. Xiao, Development and implementation of plasma sprayed nanostructured ceramic coatings, Surf. Coat. Tech. 146 (2001) 48–54.
[29] R.S. Lima, A. Kucuk, C.C. Berndt, Bimodal distribution of mechanical properties on plasma sprayed nanostructured partially stabilized zirconia, Mat. Sci. Eng. A-Struct. 327 (2002) 224–232.
[30] B. Liang, C.X. Ding, Thermal shock resistances of nanostructured and conventional zirconia coatings deposited by atmospheric plasma spraying, Surf. Coat. Tech. 197 (2005) 185–192.
[31] C.B. Liu, Z.M. Zhang, X.L. Jiang, M. Liu, Z.H. Zhu, Comparison of thermal shock behaviors between plasma-sprayed nanostructured and conventional zirconia thermal barrier coatings, T. Nonferr. Metal. Soc. 19 (2009) 99–107.
[32] W.Q. Wang, C.K. Sha, D.Q. Sun, X.Y. Gu, Microstructural feature, thermal shock resistance and isothermal oxidation resistance of nanostructured zirconia coating, Mat. Sci. Eng. A-Struct. 424 (2006) 1–5.
[33] J. Wu, H.B. Guo, L. Zhou, L. Wang, S.K. Gong, Microstructure and thermal properties of plasma sprayed thermal barrier coatings from nanostructured YSZ, J. Therm. Spray. Technol. 19 (2010) 1186–1194.
[34] R. Lima, B. Marple, Toward highly sintering-resistant nanostructured ZrO_2–7wt% Y_2O_3 coatings for TBC applications by employing differential sintering, J. Therm. Spray. Technol. 17 (2008) 846–852.
[35] R.S. Lima, B.R. Marple, Nanostructured, YSZ thermal barrier coatings engineered to counteract sintering effects, Mat. Sci. Eng. A-Struct. 485 (2008) 182–193.
[36] G.C. Kuczynski, Self-diffusion in sintering of metallic particles, T. Am. I. Min. Met. Eng. 185 (1949) pp. 169-178.
[37] F. Cernuschi, P. Bison, S. Marinetti, E. Campagnoli, Thermal diffusivity measurement by thermographic technique for the non-destructive integrity assessment of TBCs coupons, Surf. Coat. Tech. 205 (2010) 498–505.
[38] R. Mcpherson, On the formation of thermally sprayed alumina coatings, J. Mater. Sci. 15 (1980) 3141–3149.
[39] Z.L. Wu, L.Y. Ni, Q.H. Yu, C.G. Zhou, Effect of thermal exposure on mechanical properties of a plasma-sprayed nanostructured thermal barrier coating, J. Therm. Spray. Technol. 21 (2012) 169–175.
[40] G.J. Yang, Z.L. Chen, C.X. Li, C.J. Li, Microstructural and mechanical property evolutions of plasma-sprayed YSZ coating during high-temperature exposure: comparison study between 8YSZ and 20YSZ, J. Therm. Spray. Technol. 22 (2013) 1294–1302.
[41] T. Liu, X.T. Luo, X. Chen, G.J. Yang, C.X. Li, C.J. Li, Morphology and size evolution of interlamellar two-dimensional pores in plasma-sprayed $La_2Zr_2O_7$ coatings during thermal exposure at 1300 °C, J. Therm. Spray. Technol. 24 (2015) 739–748.
[42] H.J. Ratzer-Scheibe, U. Schulz, The effects of heat treatment and gas atmosphere on the thermal conductivity of APS and EB-PVD PYSZ thermal barrier coatings,

Surf. Coat. Tech. 201 (2007) 7880–7888.
[43] Y. Tan, J.P. Longtin, S. Sampath, H. Wang, Effect of the starting microstructure on the thermal properties of as-sprayed and thermally exposed plasma-sprayed YSZ coatings, J. Am. Ceram. Soc. 92 (2009) 710–716.
[44] T.W. Clyne, I.O. Golosnoy, J.C. Tan, A.E. Markaki, Porous materials for thermal management under extreme conditions, Philos. T. Roy. Soc. A 364 (2006) 125–146.
[45] I.O. Golosnoy, S.A. Tsipas, T.W. Clyne, An analytical model for simulation of heat flow in plasma-sprayed thermal barrier coatings, J. Therm. Spray. Technol. 14 (2005) 205–214.
[46] P.G. Klemens, M. Gell, Thermal conductivity of thermal barrier coatings, Mat. Sci. Eng. A-Struct. 245 (1998) 143–149.
[47] F. Cernuschi, P.G. Bison, S. Marinetti, P. Scardi, Thermophysical, mechanical and microstructural characterization of aged free-standing plasma-sprayed zirconia coatings, Acta Mater. 56 (2008) 4477–4488.
[48] J. Moon, H. Choi, H. Kim, C. Lee, The effects of heat treatment on the phase transformation behavior of plasma-sprayed stabilized ZrO_2 coatings, Surf. Coat. Tech. 155 (2002) 1–10.
[49] R.W. Trice, Y.J. Su, J.R. Mawdsley, K.T. Faber, A.R. De Arellano-Lopez, H. Wang, W.D. Porter, Effect of heat treatment on phase stability, microstructure, and thermal conductivity of plasma-sprayed YSZ, J. Mater. Sci. 37 (2002) 2359–2365.
[50] J. Ilavsky, J.K. Stalick, Phase composition and its changes during annealing of plasma-sprayed YSZ, Surf. Coat. Tech. 127 (2000) 120–129.
[51] H.G. Scott, Phase-relationships in the magnesia-yttria-zirconia system, J. Aust. Ceram. Soc. 17 (1981) 16–20.
[52] A. Shinmi, X. Zhao, P. Xiao, Mechanical and electrical characterisation of a phase transformation in thermal barrier coatings, Surf. Coat. Tech. 205 (2010) 2678–2686.
[53] S. Karthikeyan, V. Balasubramanian, R. Rajendran, Developing empirical relationships to estimate porosity and Young's modulus of plasma sprayed YSZ coatings, Appl. Surf. Sci. 296 (2014) 31–46.
[54] J. Ilavsky, G.G. Long, A.J. Allen, C.C. Berndt, Evolution of the void structure in plasma-sprayed YSZ deposits during heating, Mat. Sci. Eng. A-Struct. 272 (1999) 215–221.
[55] F. Kroupa, J. Dubsky, Pressure dependence of Young's moduli of thermal sprayed materials, Scr. Mater. 40 (1999) 1249–1254.
[56] C.J. Li, W.Z. Wang, Quantitative characterization of lamellar microstructure of plasma-sprayed ceramic coatings through visualization of void distribution, Mat. Sci. Eng. A-Struct. 386 (2004) 10–19.
[57] A. Ohmori, C.J. Li, Quantitative characterization of the structure of plasma-sprayed Al_2O_3 coating by using copper electroplating, Thin Solid Films 201 (1991) 241–252.
[58] Y. Li, C.J. Li, G.J. Yang, C.X. Li, Relation between microstructure and thermal conductivity of plasma-sprayed 8YSZ coating, Int. J. Mod. Phys. B 24 (2010) 3017–3022.
[59] T.W. Clyne, S.C. Gill, Residual stresses in thermal spray coatings and their effect on interfacial adhesion: a review of recent work, J. Therm. Spray. Technol. 5 (1996) 401–418.
[60] S.G. Chen, Y.S. Yin, D.P. Wang, X. Wang, Effect of nanocrystallite structure on the lower activation energy for Sm_2O_3-doped ZrO_2, J. Mol. Struct. 703 (2004) 19–23.
[61] E.R. Leite, T.R. Giraldi, F.M. Pontes, E. Longo, A. Beltran, J. Andres, Crystal growth in colloidal tin oxide nanocrystals induced by coalescence at room temperature, Appl. Phys. Lett. 83 (2003) 1566–1568.
[62] P. Bengtsson, T. Johannesson, Characterization of microstructural defects in plasma-sprayed thermal barrier coatings, J. Therm. Spray. Technol. 4 (1995) 245–251.
[63] Y. Wang, Y. Bai, K. Liu, J.W. Wang, Y.X. Kang, J.R. Li, H.Y. Chen, B.Q. Li, Microstructural evolution of plasma sprayed submicron-/nano-zirconia-based thermal barrier coatings, Appl. Surf. Sci. 363 (2016) 101–112.
[64] J.F. Li, C.X. Ding, Polishing-induced pull outs of plasma sprayed Cr_3C_2-NiCr coating, J. Mater. Sci. Lett. 18 (1999) 1719–1721.
[65] G.J. Yang, C.J. Li, C.X. Li, K. Kondoh, A. Ohmori, Improvement of adhesion and cohesion in plasma-sprayed ceramic coatings by heterogeneous modification of nonbonded lamellar interface using high strength adhesive infiltration, J. Therm. Spray. Technol. 22 (2013) 36–47.